

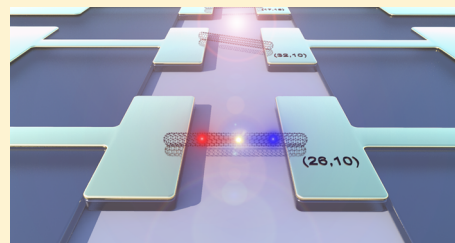
Determining the Chiral Index of Semiconducting Carbon Nanotubes Using Photoconductivity Resonances

T. DeBorde, L. Aspitarte, T. Sharf, J. W. Kevek, and E. D. Minot*

Department of Physics, Oregon State University, Corvallis, Oregon 97331, United States

S Supporting Information

ABSTRACT: We utilize photoconductivity spectroscopy to identify the unique chiral structure of individual carbon nanotubes (CNTs). Peaks in photoconductivity are measured throughout the visible and near-IR wavelength ranges. Photoconductivity peaks associated with individual CNTs are referenced against existing Rayleigh scattering measurements to uniquely identify chiral indices. We find close agreement between our assigned exciton resonances and the previously published exciton resonances. The typical net energy mismatch is ≤ 20 meV. By enabling chiral identification of CNTs after the completion of device fabrication, the technique offers a facile method for investigating relationships between CNT structure and electronic/optoelectronic properties.



INTRODUCTION

Carbon nanotubes (CNTs) are a promising platform for future electronic and optoelectronic applications.¹ For example, the electrical properties of CNTs have been exploited to build high performance transistors,² and the strong optical absorption of CNTs promise applications in energy harvesting and photo-detector devices.³

Carbon nanotubes have a rich variety of optical and electronic properties that are remarkably sensitive to chiral index. The structure–property relationships for CNTs remain an active area of investigation. For example, the nonzero bandgap of quasi-metallic CNTs is predicted to depend on chiral index.⁴ Similarly, the spin–orbit coupling in CNTs may be strongly dependent on chiral index.^{5–7} To establish structure–property relationships such as these, it is critical to have chirality characterization techniques for individual CNTs. Such techniques exist, but are challenging to implement. An early technique based on Rayleigh scattering has enabled chiral identification of individual ultralong suspended CNTs.⁸ The technique was later refined to work with individual CNTs on ultraclean surfaces.⁹ In either case, these techniques impose stringent requirements on the preparation of the CNT sample. Very recently, researchers introduced spatial modulation spectroscopy³ and polarization-based spectroscopy¹⁰ which reject background scattering and overcome the limitations of earlier techniques.

In parallel with the development of all-optical techniques, researchers have used the electrical response of CNTs to determine optical resonances. Optical instrumentation is simplified because there is no need to collect scattered or transmitted light. Several authors have observed resonances in the photocurrent spectrum of CNT pn junctions.^{11–14} Malapanis et al. have used these resonances to identify the chiral index of a CNT.¹⁴ The challenge of this technique is the fabrication of the pn junction. In earlier, complementary work,

Freitag et al. observed an optical resonance in the photoconductivity spectrum of CNT FETs.¹⁵ The peak position of a single resonance, however, was insufficient to identify chiral index.

In this work we use a broad range of excitation wavelengths to measure multiple photoconductivity resonances in 13 different suspended CNT FETs. We find close agreement between our measured resonances and the published Rayleigh scattering data that are commonly used to assign chiral index to suspended CNTs.¹⁶ The FET geometry is the most common geometry for electrical studies of CNTs, therefore, it is extremely useful to have a facile chiral identification technique that is compatible with as-fabricated CNT FETs.

EXPERIMENTAL METHOD

Existing data on CNT optical resonances was obtained using Rayleigh scattering from suspended CNTs,¹⁶ therefore, we use a similar suspended geometry to allow one-to-one comparisons between photoconductivity resonances and Rayleigh scattering. Device fabrication is described in detail by Sharf et al.¹⁷ Briefly, the device substrate is silicon wafer (p^+) with one micrometer of thermally grown oxide. Platinum/titanium electrodes (100/1 nm) are created using standard photolithography techniques. Reactive ion etching is used to produce a trench between the source-drain electrodes ($\sim 1 \mu\text{m}$ in width) with the electrode layer acting as a shadow mask during the etching process.

After creating the electrodes and trench, windows are patterned on the source/drain electrodes for deposition of the CNT growth catalyst. Electron beam physical vapor deposition is used to put down the iron catalyst pads and supporting layers (Fe/SiO₂/Ti, 1/20/1 nm). The final

Received: March 2, 2014

Revised: April 20, 2014

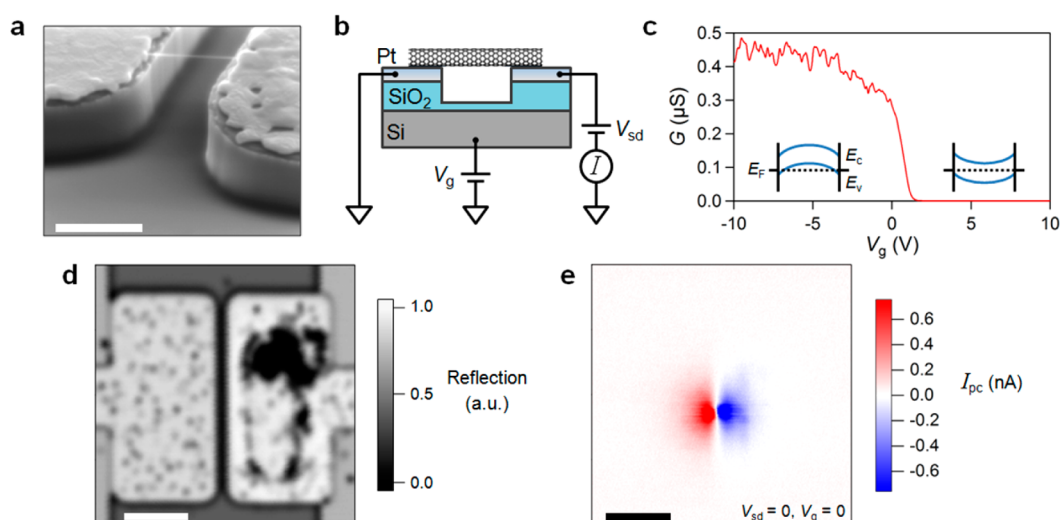


Figure 1. Suspended CNT FET device. (a) Scanning electron microscopy image of a typical device. Scale bar is 1 μm . (b) Cartoon of device geometry and circuit diagram. (c) Transistor curve of conductance versus back gate voltage, V_g , of device 1. Inset cartoons show band bending diagrams for the on and off state. (d) Reflection image of device 1. (e) Photocurrent image of device 1, $V_g = 0$ V. Photocurrent is measured with a current preamplifier connected to the right electrode; the left electrode is grounded. Scale bar in d and e is 5 μm .

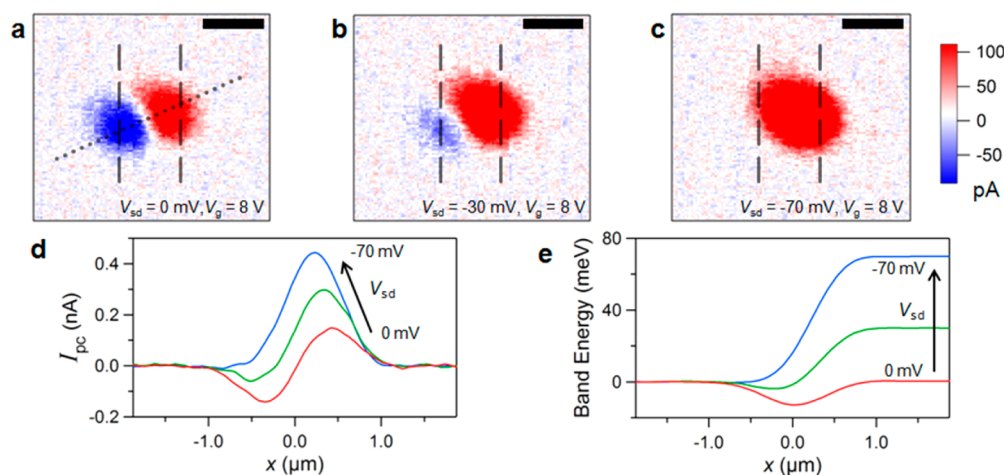


Figure 2. (a–c) Photocurrent is measured with a current preamplifier connected to the right electrode while varying the potential offset at the input (V_{sd}). The left electrode is grounded. Dashed lines in the images represent electrode edges. The scale bars are 1 μm . (d) Line cuts corresponding to the dotted line in (a) with $V_{sd} = 0, -30,$ and -70 mV. (e) Band edge energy calculated by integrating the line cuts from (d).

fabrication step is a fast-heat chemical vapor deposition growth process at 800 $^{\circ}\text{C}$, which has been shown to result in defect-free suspended CNTs.¹⁷

Wavelength-resolved scanning photocurrent microscopy (SPCM) measurements are achieved using a super continuum laser (Fianium, SC-450) that is dispersed and filtered by a monochromator (Horiba Jobin-Yvon, HRMicro). Scanning and imaging are accomplished with a pair of scan mirrors (Nutfield Tech., OHF-7, QD-4000) and a 50x objective (Nikon, CFI LU BD ELWD, NA = 0.55) coupled with a confocal lens pair (Thorlabs, Achromatic doublets). Reflection images are recorded by measuring the reflected light intensity with a silicon photodetector (Thorlabs, PDA 100A). Photocurrent is measured by a current preamplifier (SRS, model SR 570) connected to the right electrode while keeping the left electrode grounded. An instrument schematic and detailed description of the microscope can be found in DeBorde et al.¹⁸

RESULTS AND DISCUSSION

Figure 1 shows a typical suspended CNT FET. A total of 13 such devices were characterized for this study. All 13 devices have transport properties consistent with semiconducting CNTs with band gaps ≥ 0.5 eV. Figure 1c shows the transistor curve for device 1. Catalyst density and growth parameters have been tuned to favor devices with one CNT connecting the source-drain electrodes (Figure 1a). Scanning electron microscopy imaging is done after photocurrent measurements to avoid contamination. The number of connected CNTs is initially determined with SPCM imaging, which neither dirties nor damages the device.

An SPCM image of device 1 is shown in Figure 1d,e. Figure 1d is the reflection image of the device that shows the source-drain electrodes, the trench channel etched into the silicon oxide, and the catalyst deposited on the right electrode that scatters light away from the photodetector. From the reflection image, the full-width at half-maximum (fwhm) of the laser spot is estimated to be 600 nm. The photocurrent image measured

at $V_{sd} = 0$ (Figure 1e) shows two strong spots of opposite polarity surrounded by fainter semicircle halos. The strong spots are caused by a combination of photovoltaic and photothermoelectric (PTE) mechanisms, while the fainter halos are thermoelectric in origin.¹⁹

Photoconductivity measurements require nonzero V_{sd} ; therefore, we first examine the effect of V_{sd} on the photocurrent image. Figure 2 shows three photocurrent images taken with the device in the off state ($V_g = 8$ V) and $V_{sd} = 0, -30,$ and -70 mV respectively. The peak value of the photocurrent increases linearly with V_{sd} (see Supporting Information, Figure S1). Dashed lines in the images denote the positions of the electrode edges determined from the reflection data. As V_{sd} becomes more negative, the photocurrent image becomes purely positive.

To analyze the potential energy profile along the length of the CNT, we examine line cuts of the photocurrent image. Assuming $I_{PC}(x)$ is proportional to the local electric field $E_x(x)$, we integrate $I_{PC}(x)$ to find the energy of the band edge.²⁰ The proportionality factor between $I_{PC}(x)$ and $E_x(x)$ is determined by matching the total shift in band edge energy with V_{sd} . We interpret the energy profiles in Figure 2e as the band bending profile along the CNT. When $|V_{sd}| > 70$ mV, the electric field from the applied bias overwhelms any band bending caused by V_g or the metal-CNT work function difference. We conclude that $|V_{sd}| > 70$ mV is a suitable for determining the photoconductivity of the CNT.

Figure 3a shows a spectrally resolved photoconductivity measurement from device 2. The device is in the off state, $V_{sd} = -250$ mV, and the laser is defocused so that photocurrent is generated in the whole CNT. The measured photocurrent has been normalized by the wavelength-dependent laser power measured at the sample. The resonant feature is fit (solid line) with a Lorentzian peak plus a linear background (blue dashed line). The resonant peak is located near 1.73 eV and has a line width of 76 meV. The line width of this peak is similar to the line widths for photocurrent resonances reported previously (~ 60 – 100 meV).^{14,15,21} Figure 3b shows the laser power dependence of the photoconductivity on resonance. In this power range, the data displays a linear dependence on incident laser power. We have also measured the polarization dependence of the photoconductivity signal both on and off resonance. The on-resonance signal shows strong polarization anisotropy, while the off-resonance signal shows weak polarization anisotropy (Figure 3c), similar to previous measurements of CNT photoconductivity and CNT pn junctions.^{13,15,21,22} Resonant peaks such as Figure 3a are strongest when polarization is parallel to the CNT axis (see Supporting Information, Figure S2).

To establish the excitonic nature of photoconductivity resonances, and to identify chiral index, we measured photoconductivity across a wide range of photon energies. Figure 4 shows the photoconductivity spectra of seven different CNT FET devices. Photon energy was typically swept from 1.4–2.7 eV (in one case, the energy range is 1.5–2.7 eV). The data is fit (solid lines) with a combination of Lorentzian functions plus a linear baseline.

Figure 4 shows evidence of both exciton resonances and phonon sidebands. The peak positions of the dominant resonances in Figure 4 are consistent with resonant Rayleigh scattering data (chiral index assignments are shown in Figure 4).¹⁶ The line widths of the resonant features are also consistent with previous studies. Typical line width are 50,

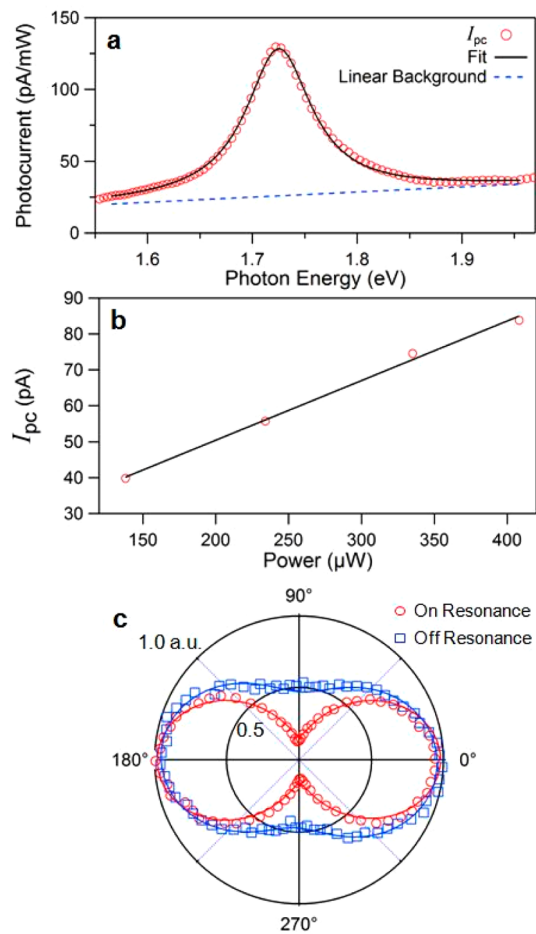


Figure 3. (a) Photoconductivity resonance measured from device 2 with $V_g = 8$ V and $V_{sd} = -250$ mV. The measured photocurrent has been normalized by incident laser power. Data is shown as red circles and is fit (solid line) with a Lorentzian peak plus a linear background (blue dashed line). (b) Photocurrent versus incident laser power measured on resonance (1.72 eV). (c) Polarization dependence of photocurrent measured from device 3 on and off resonance at 1.77 and 1.94 eV, respectively (see Supporting Information Figure S2). The photocurrent was measured with $V_g = 5$ V, $V_{sd} = 100$ mV.

70, and 150 meV for E_{33} , E_{44} , and E_{55} peaks, respectively. Comparing E_{33} resonances among different CNTs shows a correlation between the resonant energy and the line width: higher resonant energy corresponds to broader line width. The same trend is seen for E_{44} , and E_{55} (see Supporting Information). The observed line widths are consistent with lifetime limited broadening and exciton lifetimes < 50 fs.^{23,24} Phonon sidebands are manifested as small satellite peaks approximately 200 meV above the larger exciton peaks (marked with asterisks in Figure 4).^{21,25}

Figure 5 shows the exciton peak positions from Figure 4, as well as five additional devices. The lower panel of Figure 5 is a Kataura plot showing the atlas of E_{ii} values (gray circles),¹⁶ with our measured photoconductivity resonances plotted on top (colored empty circles). For each measured CNT, the chiral index assignment was made by identifying the closest match in the CNT atlas. To characterize the goodness of fit, we determine a residual energy parameter, E_{res}

$$E_{res}^2 = \sum_i (E_{ii,PC} - E_{ii,Atlas})^2 \quad (1)$$

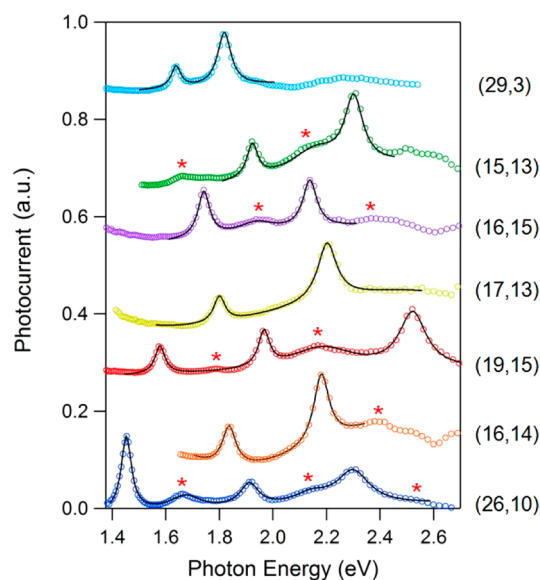


Figure 4. Photoconductivity spectra of CNT FET devices. Photoconductivity spectra have been normalized with incident laser power spectra measured at the sample position and have also been rescaled to be plotted together. Measured data is shown as colored circles and fit by Lorentzian peaks plus linear backgrounds (black lines). Smaller peaks that are consistent phonon sideband resonances are marked with red asterisks. Chiral indices are displayed on the right of each trace.

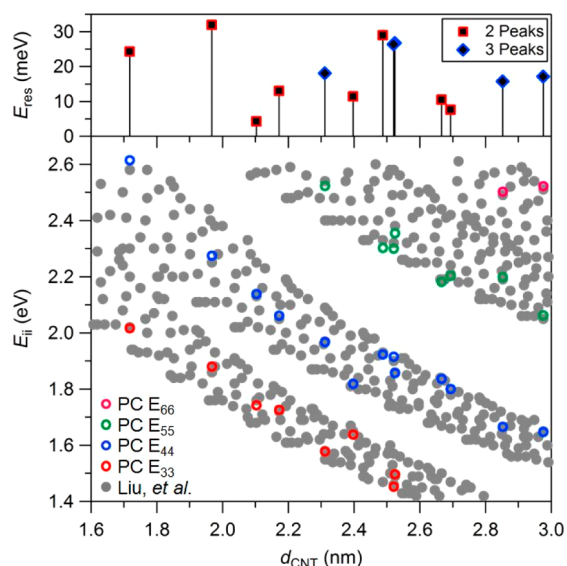


Figure 5. Top panel shows the energy residual parameter, E_{res} , calculated from eq 1. The corresponding photoconductivity resonances and atlas data are shown directly underneath each energy residual. E_{res} values calculated from two peaks are represented with squares. E_{res} values calculated from three peaks are represented with diamonds. The bottom panel shows the previously published set of exciton resonances for semiconducting CNTs (filled gray circles)¹⁶ with measured photoconductivity resonances plotted as empty, colored circles.

where $E_{\text{ii,PC}}$ and $E_{\text{ii,Atlas}}$ refer to the measured photoconductivity peaks and the reference resonances, respectively.¹⁶ E_{res} is the distance in energy space between the measured exciton resonances and the nearest match in the CNT atlas. Confident chirality assignment requires minimization of E_{res} . All of the measured CNTs have an E_{res} value below 35 meV, while the

majority of the matches yield E_{res} below 20 meV. This is the same level of experimental uncertainty reported in Rayleigh scattering experiments.¹⁶

The close agreement between our measured peak positions and Rayleigh scattering data suggests that the resonances have the same origin, namely resonant exciton generation. It appears that the photoconductivity spectra of CNT FETs (this work and refs 15 and 21) the photocurrent spectra of CNT pn junctions,^{11–14} and Rayleigh scattering,^{8,9,16} all yield the same spectral fingerprint.

CONCLUSION

In conclusion, we have measured photoconductivity spectra of suspended semiconducting CNT FETs and observe good agreement with resonant Rayleigh scattering measurements. The chiral indices of a CNT can be identified by matching its photoconductivity spectra to the atlas of CNT exciton resonances.¹⁶ While this work utilizes devices with 1 μm channel length, the spectrally resolved photoconductivity technique is suitable for any channel length, from tens of nanometers to tens of micrometers. The technique can be applied to as-fabricated CNT devices and requires minimal optical instrumentation.

ASSOCIATED CONTENT

Supporting Information

Measurement of the linear dependence of peak photocurrent on source-drain bias. Photoconductivity spectra measured with incident polarization aligned either parallel or perpendicular to the CNT axis. Corroborative resonant Raman spectroscopy measurement of carbon nanotube radial breathing mode. Table summarizing all measured carbon nanotube photoconductivity resonances. Graph showing full-width at half-maximum dependence on transition energy. This material is available free of charge via the Internet at <http://pubs.acs.org>.

AUTHOR INFORMATION

Corresponding Author

*E-mail: minote@science.oregonstate.edu. Phone: 1-541-737-9671.

Notes

The authors declare no competing financial interest.

ACKNOWLEDGMENTS

This material is based upon work supported by the National Science Foundation under Grant No. 1151369. Sample fabrication was performed in part at the MaSC Facility at Oregon State University. This work was performed in part at the Cornell NanoScale Facility, a member of the National Nanotechnology Infrastructure Network, which is supported by the National Science Foundation (Grant ECCS-0335765).

REFERENCES

- (1) Avouris, P.; Chen, J. Nanotube Electronics and Optoelectronics. *Mater. Today* **2006**, *9*, 46–54.
- (2) Franklin, A. D.; et al. Carbon Nanotube Complementary Wrap-Gate Transistors. *Nano Lett.* **2013**, *13*, 2490–2495.
- (3) Blancon, J.-C.; et al. Direct Measurement of the Absolute Absorption Spectrum of Individual Semiconducting Single-Wall Carbon Nanotubes. *Nat. Commun.* **2013**, *4*, 2542–2542.
- (4) Deshpande, V. V.; Chandra, B.; Caldwell, R.; Novikov, D. S.; Hone, J.; Bockrath, M. Mott Insulating State in Ultraclean Carbon Nanotubes. *Science* **2009**, *323*, 106–110.

- (5) Pei, F.; Laird, E. A.; Steele, G. A.; Kouwenhoven, L. P. Valley-Spin Blockade and Spin Resonance in Carbon Nanotubes. *Nat. Nano* **2012**, *7*, 630–634.
- (6) Cleuziou, J. P.; N'Guyen, N. V.; Florens, S.; Wernsdorfer, W. Interplay of the Kondo Effect and Strong Spin-Orbit Coupling in Multihole Ultraclean Carbon Nanotubes. *Phys. Rev. Lett.* **2013**, *111*, 136803.
- (7) Pecker, S.; Kuemmeth, F.; Secchi, A.; Rontani, M.; Ralph, D. C.; McEuen, P. L.; Ilani, S. Observation and Spectroscopy of a Two-Electron Wigner Molecule in an Ultraclean Carbon Nanotube. *Nat. Phys.* **2013**, *9*, 576–581.
- (8) Sfeir, M. Y.; Wang, F.; Huang, L.; Chuang, C.-C.; Hone, J.; O'Brien, S. P.; Heinz, T. F.; Brus, L. E. Probing Electronic Transitions in Individual Carbon Nanotubes by Rayleigh Scattering. *Science (New York, N.Y.)* **2004**, *306*, 1540–1543.
- (9) Joh, D. Y.; Herman, L. H.; Ju, S.-Y.; Kinder, J.; Segal, M. a.; Johnson, J. N.; Chan, G. K. L.; Park, J. On-Chip Rayleigh Imaging and Spectroscopy of Carbon Nanotubes. *Nano Lett.* **2011**, *11*, 1–7.
- (10) Liu, K.; et al. High-Throughput Optical Imaging and Spectroscopy of Individual Carbon Nanotubes in Devices. *Nat. Nanotechnol.* **2013**, *8*, 917–922.
- (11) Lee, J. U.; Codella, P. J.; Pietrzykowski, M., Direct Probe of Excitonic and Continuum Transitions in the Photocurrent Spectroscopy of Individual Carbon Nanotube P–N Diodes. *Appl. Phys. Lett.* **2007**, *90*.
- (12) Gabor, N. M.; Zhong, Z. H.; Bosnick, K.; Park, J.; McEuen, P. L. Extremely Efficient Multiple Electron-Hole Pair Generation in Carbon Nanotube Photodiodes. *Science* **2009**, *325*, 1367–1371.
- (13) Barkelid, M.; Steele, G. A.; Zwiller, V. Probing Optical Transitions in Individual Carbon Nanotubes Using Polarized Photocurrent Spectroscopy. *Nano Lett.* **2012**, *12*, 5649–5653.
- (14) Malapanis, A.; Perebeinos, V.; Sinha, D. P.; Comfort, E.; Lee, J. U. Quantum Efficiency and Capture Cross Section of First and Second Excitonic Transitions of Single-Walled Carbon Nanotubes Measured through Photoconductivity. *Nano Lett.* **2013**, *13*, 3531–3538.
- (15) Freitag, M.; Martin, Y.; Misewich, J. A.; Martel, R.; Avouris, P. H. Photoconductivity of Single Carbon Nanotubes. *Nano Lett.* **2003**, *3*, 1067–1071.
- (16) Liu, K.; et al. An Atlas of Carbon Nanotube Optical Transitions. *Nat. Nanotechnol.* **2012**, *7*, 325–329.
- (17) Sharf, T.; Kevek, J. W.; DeBorde, T.; Wardini, J. L.; Minot, E. D. Origins of Charge Noise in Carbon Nanotube Field-Effect Transistor Biosensors. *Nano Lett.* **2012**, *12*, 6380–6384.
- (18) DeBorde, T.; Kevek, J. W.; Sharf, T.; Wardini, J. L.; Minot, E. D. A Spectrally-Tunable Photocurrent Microscope for Characterizing Nanoelectronic Devices. In *2011 11th IEEE Conference on Nanotechnology (IEEE-NANO)*, Portland, OR, 15–18 Aug. 2011; IEEE: New York, 2011; pp 382–386.
- (19) DeBorde, T.; Aspitarte, L.; Sharf, T.; Kevek, J. W.; Minot, E. D. Photothermoelectric Effect in Suspended Semiconducting Carbon Nanotubes. *ACS Nano* **2014**, *8*, 216–221.
- (20) Ahn, Y. H.; Tsen, A. W.; Kim, B.; Park, Y. W.; Park, J. Photocurrent Imaging of P–N Junctions in Ambipolar Carbon Nanotube Transistors. *Nano Lett.* **2007**, *7*, 3320–3323.
- (21) Qiu, X. H.; Freitag, M.; Perebeinos, V.; Avouris, P. Photoconductivity Spectra of Single-Carbon Nanotubes: Implications on the Nature of Their Excited States. *Nano Lett.* **2005**, *5*, 749–752.
- (22) Freitag, M.; Tsang, J. C.; Bol, A.; Yuan, D. N.; Liu, J.; Avouris, P. Imaging of the Schottky Barriers and Charge Depletion in Carbon Nanotube Transistors. *Nano Lett.* **2007**, *7*, 2037–2042.
- (23) Ma, Y.-Z.; Stenger, J.; Zimmermann, J.; Bachilo, S. M.; Smalley, R. E.; Weisman, R. B.; Fleming, G. R. Ultrafast Carrier Dynamics in Single-Walled Carbon Nanotubes Probed by Femtosecond Spectroscopy. *J. Chem. Phys.* **2004**, *120*, 3368–3373.
- (24) Manzoni, C.; Gambetta, a.; Menna, E.; Meneghetti, M.; Lanzani, G.; Cerullo, G. Intersubband Exciton Relaxation Dynamics in Single-Walled Carbon Nanotubes. *Phys. Rev. Lett.* **2005**, *94*, 207401–207401.
- (25) Berciaud, S.; Voisin, C.; Yan, H.; Chandra, B.; Caldwell, R.; Shan, Y.; Brus, L. E.; Hone, J.; Heinz, T. F. Excitons and High-Order